Front. Phys. 12(3), 128702 (2017)
DOI 10.1007/s11467-017-0670-1

RESEARCH ARTICLE

Regulation of 1, 4, 5-triphosphate receptor channel gating dynamics by mutant presenilin in Alzheimer's disease cells

Fang Wei[1], **Xiang Li**[2], **Meichun Cai**[1], **Yanping Liu**[1], **Peter Jung**[3], **Jianwei Shuai**[1,2,4,†]

[1] *Department of Physics, Xiamen University, Xiamen 361005, China*
[2] *State Key Laboratory of Cellular Stress Biology, Innovation Center for Cell Signaling Network,*
School of Life Sciences, Xiamen University, Xiamen 361005, China
[3] *Department of Physics and Astronomy and Quantitative Biology Institute, Ohio University, Athens, OH 45701, USA*
[4] *Research Institute for Biomimetics and Soft Matter, Fujian Provincial Key Laboratory for Soft Functional*
Materials Research, Xiamen University, Xiamen 361005, China
Corresponding author. E-mail: †jianweishuai@xmu.edu.cn

Received October 31, 2016; accepted January 18, 2017

In neurons of patients with Alzheimer's disease, the intracellular Ca^{2+} concentration is increased by its release from the endoplasmic reticulum via the inositol 1, 4, 5-triphosphate receptor (IP_3R). In this paper, we discuss the IP_3R gating dynamics in familial Alzheimer's disease (FAD) cells induced with presenilin mutation PS1. By fitting the parameters of an IP_3R channel model to experimental data of the open probability, the mean open time and the mean closed time of IP_3R channels, in control cells and FAD mutant cells, we suggest that the interaction of presenilin mutation PS1 with IP_3R channels leads the decrease in the unbinding rates of IP_3 and the activating Ca^{2+} from IP_3Rs. As a result, the increased affinities of IP_3 and activating Ca^{2+} for IP_3R channels induce the increase in the Ca^{2+} signal in FAD mutant cells. Specifically, the PS1 mutation decreases the IP_3 dissociation rate of IP_3R channels significantly in FAD mutant cells. Our results suggest possible novel targets for FAD therapeutic intervention.

Keywords Ca^{2+} signal, channel, neuron, Alzheimer's disease

PACS numbers 87.15.A-, 87.15.hj

1 Introduction

Alzheimer's disease (AD) is a common chronic disease involving the slow destruction of neurons, resulting in serious cognition disorders. Most AD is sporadic and occurs after the age of 60 years. About 10% of AD develops before the age of 60 years, and is termed autosomal dominant familial Alzheimer's disease (FAD). Although familial and sporadic ADs are different in their age of onset, they have the same symbolic characteristics, including extracellular age-related pigment deposition by the β amyloid protein and neurofibrillary tangles in neurons by Tau protein hyperphosphorylation [1–4], indicating the same etiology for both familial and sporadic AD. According to the β-amyloid (Aβ) cascade hypothesis of AD pathogenesis, mutations of amyloid precursor protein (APP) and presenilin lead to abnormal secretion and abundance of Aβ. The Aβ proteins deposited in the brain tissue are toxic to the neurons and synapses, and can destroy synaptic membranes, causing neuronal death [5, 6]. It has been suggested that APP and presenilin mutations PS1 and PS2 are the main causes of FAD [1].

While extracellular Aβ can influence the steady state concentrations of intracellular Ca^{2+} both *in vitro* and *in vivo*, FAD presenilin mutations can also affect intracellular Ca^{2+} concentrations via an intracellular mechanism [7, 8]. In AD neurons, the increased Ca^{2+} concentration is caused mainly by an increase in Ca^{2+} release from the endoplasmic reticulum (ER) [9–13]. In response to

---

*Special Topic: Soft-Matter Physics and Complex Systems (Ed. Zhi-Gang Zheng).

the second messenger inositol 1, 4, 5-triphosphate (IP_3), release of Ca^{2+} from the ER through the IP_3 receptor channels (IP_3R) is a common mechanism and has been observed in many cells [14]. A proper increase in the cytosolic Ca^{2+} concentration plays a pivotal role in regulating many intracellular functions, for example in learning and memory [15].

Several molecular mechanisms have been suggested for the increased cytosolic Ca^{2+} in AD neurons. It might be related to the enhanced ability to store Ca^{2+} in the ER lumen, such as via the enhanced sarcoendoplasmic reticulum Ca^{2+}-ATPase (SERCA) pump [16]. Other hypothesized mechanisms for the increased cytosolic Ca^{2+} concentration include the increased release of Ca^{2+} through IP_3Rs [10, 12] or ryanodine receptors (RyR) [11, 17, 18], an increased abundance of channels, and an enhanced affinity of IP_3R for its ligand IP_3. The increased cytosolic Ca^{2+} signals might be also caused by a decrease of the ER-mitochondrial distance [19, 20]. In fact, the increased Ca^{2+} concentration is used to diagnose FAD [21, 22].

Recently, Cheung *et al.* studied how the biochemical interaction of FAD mutant PS1(M146L)/PS2 with the IP_3Rs affects the intracellular Ca^{2+} signal in response to IP_3 stimulation [23, 24]. They indicated that, compared with the wild-type PS, the interaction of FAD mutant PS with the IP_3R channels profoundly enhanced the gating activity of the IP_3R, resulting in the increased intracellular Ca^{2+} levels. However, the details of how the mutant PS influences the gating dynamics of Ca^{2+} and IP_3 binding to and unbinding from IP_3Rs are unclear and remain a challenging experimental problem. Understanding the modulation of the ligand binding and unbinding properties of IP_3Rs by mutant PS is important for the design of novel targets for therapeutic intervention. In this study, we used computational modeling of IP_3Rs to investigate how the IP_3R gating dynamics are influenced by FAD mutant PS1.

Various mathematical models of IP_3R have been used to study IP_3R gating dynamics. DeYoung and Keizer put forward a model (the DYK model) where the entire channel is made up of three identical and independent subunits [25], each of which have binding sites for IP_3 and Ca^{2+} (see below for more detail). Sneyd and Dufour considered a specific kinetic model for the type-2 IP_3R by asserting that the channel functions as one entity rather than as four subunits [26]. Mak *et al.* proposed an allosteric four-plus-two conformation model in which the IP_3R comprises four identical and independent IP_3R monomers [27]. Shuai *et al.* suggested a modified De Young–Keizer model, taking into account the four independent subunits and considering IP_3R opening through a configuration change [28]. Further IP_3R models are discussed and compared by Shuai *et al.* [29]. Ullah *et al.* established a data-driven model, comprising a Markov chain with nine closed states and three open states, to discuss the modal gating behavior [30]. More recently, a model with four independent subunits was proposed [31] to account for equilibrium channel properties, transient responses to changing ligand conditions, and modal gating statistics [32, 33], showing that cooperative binding or concerted conformational changes are not required for IP_3R modal gating.

In this study, we adopted a simulated annealing algorithm to optimize the parameters in a modified DYK model by fitting the experimental results of open probability P_O, mean open time τ_O, and mean closed time τ_C in wild-type PS1-expressing Sf9 cells (control cells) and in FAD mutant PS1-M146L-expressing cells (M146L cells). The results of comparing the parameter distributions between IP_3R models for the control and M146L cells suggested that the affinities of IP_3R channels for IP_3 and the activating Ca^{2+} both increase in the cell with mutated PS1, leading to the increased Ca^{2+} release.

2 Method and model

2.1 Experimental data for IP_3R

The experimental data of the IP_3R gating dynamics influenced by FAD mutations in PS were obtained at various Ca^{2+} concentrations (C) and IP_3 concentrations (I) in *Spodoptera frugiperda* (Sf9), DT40 cells, human B lymphoblasts, and mouse cortical neurons [23, 24]. Using the membrane patch clamp technique, the IP_3R gating parameters, including open probability P_O, mean open time τ_O, and mean closed time τ_C, were obtained. Compared with the IP_3R gating dynamics in wild-type PS1-expressing cells, the open probabilities P_O of IP_3R channels in FAD mutant PS1-M146L-expressing cells increase significantly at all IP_3 concentrations. The corresponding mean open time τ_O increases too, while the mean closed time τ_C decreases.

As an example for SF9 cells, at $C = 1$ μM and $I = 10$ μM, $P_O = 0.76 \pm 0.05$ in the control cells, while $P_O = 0.86 \pm 0.03$ in the M146L cells [23]. At an intracellular calcium concentration of $C = 1$ μM and an IP_3 concentration of $I = 33$ nM, the relevant open probabilities are $P_O = 0.27 \pm 0.01$ for the control cells, and $P_O = 0.75 \pm 0.06$ for the M146L cells. Interestingly, the open probabilities at low IP_3 concentrations in the M146L cells were nearly equal to those at saturating IP_3 concentration in the control cells. Subsequently, by fitting the experimental data to a modified DYK IP_3R model, we discuss in detail how the mutant PS1 affects the binding and dissociation dynamics of Ca^{2+} and IP_3 for an IP_3R channel.

2.2 The IP$_3$R model

To date, many different IP$_3$R channel models have been suggested [25–31]. In the present study, we adopted a modified version of the DYK model [28], in which each parameter has a direct biological meaning related to Ca^{2+} or IP$_3$ ligand binding or association with the channel. The modified DYK IP$_3$R model comprises four subunits. In each subunit, there are three binding sites: an IP$_3$ binding site, an activating Ca^{2+} binding site, and an inhibitory Ca^{2+} binding site. The state of each subunit is denoted by the triplet index (ijk), where index i represents the state of the IP$_3$ binding site, j the state of the activating Ca^{2+} binding site, and k the state of the inhibitory Ca^{2+} binding site. An occupied site is represented by 1, and a non-occupied site by 0, giving rise to eight possible states for each subunit (Fig. 1). The subunit is active when it is bound with IP$_3$ and activating Ca^{2+}, but not inhibitory Ca^{2+}, i.e., if it is in the state (110). The channel is open when there are three or four subunits in the active state (110).

As indicated in Fig. 1, the transitions between the eight states are governed by the second-order rate constants a_i for the binding processes and by the first-order rate constant b_i for the unbinding processes. The dissociation constants, i.e., $d_i = b_i/a_i$, should satisfy $d_1d_2 = d_3d_4$ because of the detailed balance. In Fig. 1, C and I represent the concentrations of Ca^{2+} and IP$_3$ in the cytoplasm, respectively.

According to the schematic diagram, we can calculate the unnormalized equilibrium probabilities q_{ijk} of each state, which are described by the ratio of binding and dissociation constants along the shortest binding/unbinding path relative to the state (000), i.e., $q_{000} = 1$, $q_{001} = \frac{C}{d_4}$, $q_{010} = \frac{C}{d_5}$, $q_{011} = \frac{C^2}{d_4d_5}$, $q_{100} = \frac{I}{d_3}$, $q_{101} = \frac{IC}{d_2d_3}$, $q_{110} = \frac{IC}{d_3d_5}$, and $q_{111} = \frac{IC^2}{d_2d_3d_5}$ [29]. The normalized equilibrium probability for state (110) then reads

$$w_{110} = \frac{q_{110}}{Z}, \tag{1}$$

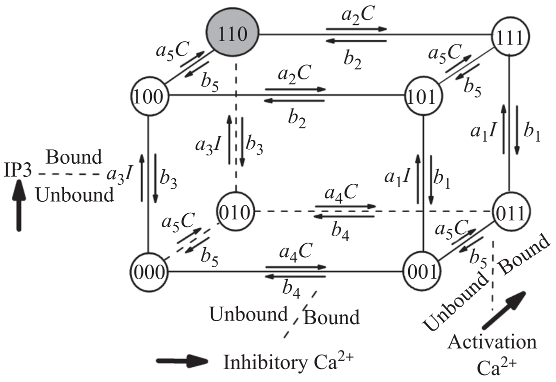

Fig. 1 Schematic diagram of the state transitions for the DYK IP$_3$R subunit. C and I represent the concentrations of Ca^{2+} and IP$_3$ in the cytoplasm, respectively

where Z is the normalization factor defined by the sum $Z = \sum_{ijk} q_{ijk}$.

Because the channel opens when at least three of the four subunits are in state (110), the open probability P_O of IP$_3$R channel is given by

$$P_O = P_{4O} + P_{3O} = w_{110}^4 + 4w_{110}^3(1 - w_{110}). \tag{2}$$

The closed states (010, 100, 111) are the only states that directly connect to the active states, the equilibrium probability flux J can be written as follows [29]:

$$J = 3P_{3O}(b_3 + b_5 + a_2C). \tag{3}$$

The mean open time τ_O, and mean close time τ_C are then given by

$$\tau_O = \frac{P_O}{J}, \tag{4}$$

$$\tau_C = \frac{1 - P_O}{J}. \tag{5}$$

As a result, the open probability P_O is only related to all dissociation constants d_i. While the mean open time τ_O and mean closed time τ_C of the channel are further related to the binding constant a_2, and the unbinding constants b_3 and b_5. Thus, the parameters d_1, d_2, d_3, d_4, d_5, a_2, b_3, and b_5 of the IP$_3$R model can be determined by the experimental data for P_O, τ_O, and τ_C. Considering $d_1d_2 = d_3d_4$, we calculated $d_1 = d_3d_4/d_2$ and then searched for the seven parameters d_2, d_3, d_4,d_5, a_2, b_3, and b_5.

2.3 Annealing algorithm

We adopt a simulated annealing algorithm to optimize these seven model parameters by fitting the experimental data of P_O, τ_O, and τ_C of the control and M146L cells given in Refs. [23, 24]. In our simulated annealing algorithm, the optimization functions are defined as

$$E_{P_O} = \frac{\Sigma_{I,C}|P_O^{\text{expt}}(I,C) - P_O^{\text{mod}}(I,C)|}{\Sigma_{I,C}P_O^{\text{expt}}(I,C)}, \tag{6}$$

$$E_\tau = \frac{\Sigma_{I,C}|\log(\tau_O^{\text{expt}}) - \log(\tau_O^{\text{mod}})|}{\Sigma_{I,C}\log(\tau_O^{\text{expt}})} + \frac{\Sigma_{I,C}|\log(\tau_C^{\text{expt}}) - \log(\tau_C^{\text{mod}})|}{\Sigma_{I,C}\log(\tau_C^{\text{expt}})}, \tag{7}$$

in which the superscript “expt” indicates the experimental data, and superscript “mod” indicates the modeling data.

Before optimizing the seven parameters, we had to define the search ranges of these parameters. Considering that the channel opens above a minimal concentration of $I = 10$ nM, we set the search range of d_3 as between 10^{-3} to 10^{-1} μM. The channel can open when C is lower than

0.1 μM; therefore, we set the search range of d_5 to 0.01 to 1 μM. In the model, there are two dissociation constants for inhibitory Ca^{2+} binding, i.e., d_2 and d_4. It has been suggested that the binding rate of inhibitory Ca^{2+} without bound IP_3 is slower than that with bound IP_3 [28], indicating that the parameter d_2 should be larger than d_4. Thus the search ranges for d_2 and d_4 were 1–100 μM and 0.1–100 μM, respectively. Inhibitory Ca^{2+} is bound only when the Ca^{2+} concentration is high; therefore, the binding rate a_2 of inhibitory Ca^{2+} was set as 10^{-3}–10 μM·s^{-1}, while the unbinding rates b_5 and b_3 of activating Ca^{2+} and IP_3 were set in the biologically reasonable range of 10^{-3}–10^3 s^{-1}.

With the decreasing temperature in the ensuing simulated annealing algorithm, the seven model parameters were updated iteratively, resulting in decreasing values of the optimization functions. Once the values of the optimization functions became smaller than a critical value, the current values of the model parameters were then identified as the optimal parameters. In our annealing algorithm, we first applied Eq. (6) with the experimental data of P_O to determine the optimal dissociation constants d_2, d_3, d_4, d_5, and then applied Eq. (7) with the data of τ_O and τ_C to determine the optimal rates a_2, b_3, b_5.

3 Results and discussion

3.1 Efficiency of the annealing algorithm to fit the model parameters

A set of optimal parameters of d_i can be obtained using our annealing algorithm. As an example, shown in Fig. 2, P_O is plotted versus C at different levels I with $d_2 = 27.0$ μM, $d_3 = 0.01$ μM, $d_4 = 0.9$ μM, and $d_5 = 0.28$ μM (which are typical parameters given in Table 1). The experimental data for the control cells are indicated by symbols. Clearly, the experimental data can be fitted well with the IP_3R parameters obtained by the simulated annealing algorithm, although the quality of the fit is not completely perfect, especially for the low IP_3 concentration of 0.01 μM. These experimental data are statistical values averaged with various IP_3R channels in different cells. In our simulation, 27 experimental data of P_O at different C and I are fitted by four parameters of d_i. Here we are not trying to find out a set of best parameters to fit the experimental data, but to find many sets of good parameters with a small, but not too small, critical values of E_{P_O} in Eq. (6), and then to discuss the distributions of these optimal parameters. We

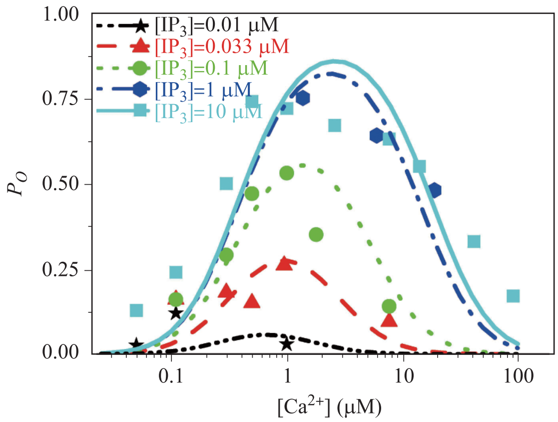

Fig. 2 Dependence of the open probability Po as a function of Ca^{2+} concentration for different IP_3 concentrations in control cells. Different colors represent different IP_3 concentrations [IP_3]. The solid symbols are the experimental results [27], and the lines are the modeling results.

Table 1 A set of typical parameter values for the modified De Young–Keizer model. The bold parameters are the parameters modulated by mutant PS1.

Binding site	Parameters	Values in the control cells	Values in the M146L cells
IP_3binding site	a_3	15.0 μM^{-1}·s^{-1}	15.0 μM^{-1}·s^{-1}
	$\boldsymbol{b_3}$	**0.15 s^{-1}**	**0.0225 s^{-1}**
	$\boldsymbol{d_3}$	**0.01 μM**	**0.0015 μM**
	$\boldsymbol{d_1}$	**0.3 μM**	**0.045 μM**
Activating Ca^{2+} binding site	a_5	126.43 μM^{-1}·s^{-1}	126.43 μM^{-1}·s^{-1}
	$\boldsymbol{b_5}$	**35.4 s^{-1}**	**22.76 s^{-1}**
	$\boldsymbol{d_5}$	**0.28 μM**	**0.18 μM**
Inhibitory Ca^{2+} binding site	a_2	0.05 μM^{-1}·s^{-1}	0.05 μM^{-1}·s^{-1}
	b_2	1.35 s^{-1}	1.35 s^{-1}
	d_2	27.0 μM	27.0 μM
	d_4	0.9 μM	0.9 μM

assume that the distributions of these optimal parameters obtained with the model reflect, to a certain extent, the variability of biological parameters of various IP_3R channels in different cells.

3.2 Range of optimal dissociation constants

Two thousand independent simulated annealing runs were carried out, generating 2000 sets of optimal parameters $\{d_i\}$. Figure 3(a) shows scatter plots of all obtained optimal values of $d_1 \ldots d_5$. Note that d_1 is calculated with $d_1 = d_3 d_4 / d_2$. Blue symbols indicate parameter values obtained from control cells, while red symbols indicate parameter values of the M146L cells. For parameter d_3, which is related to IP_3 binding, the scatter ranges have no overlap between the control and M146L cells. In contrast, the ranges of d_4 are almost identical in the two kinds of cells. In addition, the ranges of d_2 and d_5 in the two types of cells have significant overlaps.

Besides the scatter ranges, we further studied the probability distributions of these optimal parameters, as shown in Figs. 4 (a)–(d) for d_i ($i = 2, 3, 4, 5$). Figure 4(a) shows that the tri-modal probability distributions of d_2 are quite similar for the control and mutant cells. The

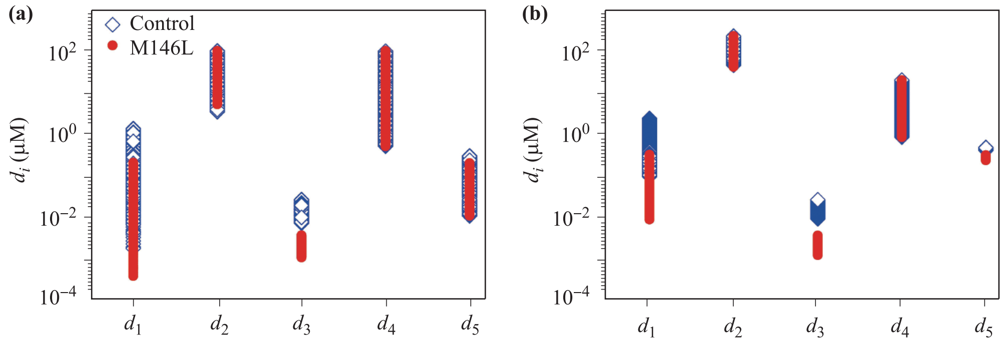

Fig. 3 Comparison of the scattering ranges of dissociation constants d_i between the control and M146L cells. **(a)** 2000 sets of optimal parameters obtained using the annealing algorithm and **(b)** filtered optimal parameters with probabilities larger than 3%. The discrete dots at horizontal axis represent d_i. The open squares represent the control cells and the filled circles represent the M146L cells.

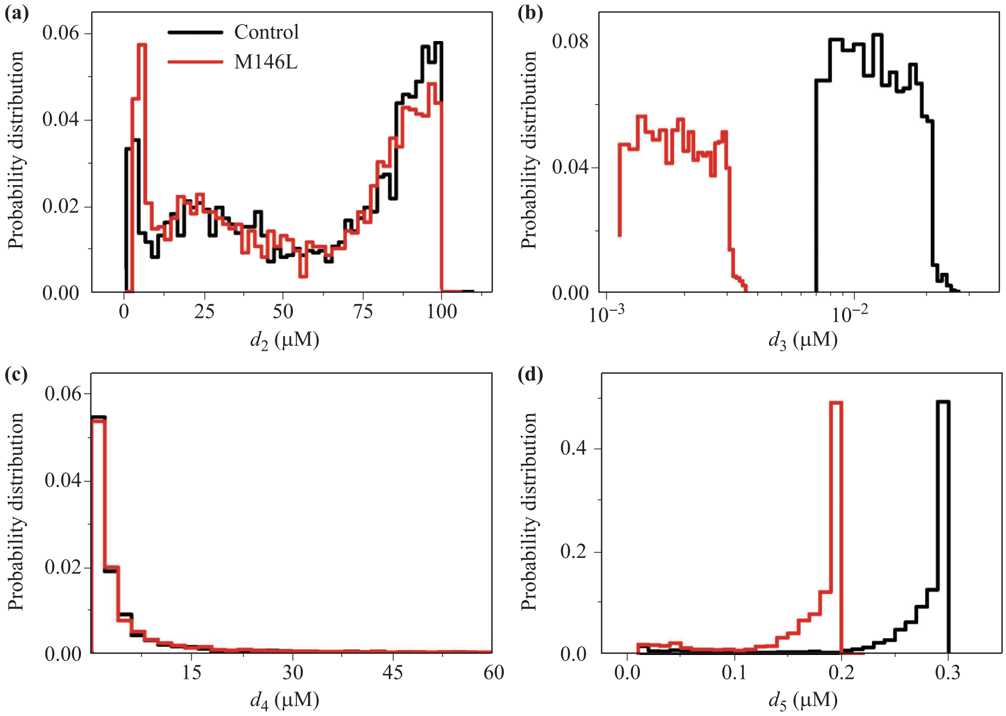

Fig. 4 Comparison of the probability distributions of dissociation constants d_i between the control and M146L cells. **(a–d)** show the parameter distributions of d_2, d_3, d_4, and d_5, respectively. The black lines represent the control cells and the red lines represent the M146L cells.

probability distributions of d_3 for the control (black) and the mutant cells (red) are disjointed [see Fig. 4(b)]. The distributions of optimal values for d_4 are almost identical for the control and mutant cells [see Fig. 4(c)]. Although the scatter ranges of d_5 overlap strongly for the control and mutant cells [Fig. 3(a)], Figure 4(d) indicates that their probability distributions are almost disjointed. In conclusion, FAD mutant PS1 expression influences IP_3Rs mainly by affecting the values of d_3 and d_5, rather than d_2 and d_4.

Figure 4 also shows that the probability distributions of the optimal parameter values can be quite small for wide ranges of parameters, especially for d_4 and d_5. Considering the robustness of the model parameters, we removed the values with small probabilities and retained those values with large probabilities. Each set of parameters was obtained within a group using our annealing algorithm; therefore, we deleted all sets of optimal parameters where one parameter value has a probability of less than 0.05. Using the remaining parameters, we replotted the scatter ranges of the parameters in Fig. 3(b) and the probability distributions in Figs. 5(a)–(d).

Figure 3(b) indicates that the scatter ranges of the filtered parameters become narrower for the two types of cells. The differences between the two cell types are more pronounced for the pruned probability distribution shown in Fig. 5. The two dissociation constants for Ca^{2+}-induced inhibition, d_2 with IP_3-bound and d_4 without IP_3-bound, display almost the same distributions for the control and the mutant cells. However, the dissociation constants d_3 and d_5 for IP_3-binding and calcium binding to the inhibitory binding site are quite different for the control and M146L cells, which are both systematically smaller in the mutant cells.

As a result of selecting the parameters from their pruned probability distributions, a set of typical parameters of $d_1 = 0.3$ μM, $d_2 = 27.0$ μM, $d_3 = 0.01$ μM, $d_4 = 0.9$ μM, and $d_5 = 0.28$ μM are suggested for the control cells (Fig. 2); and $d_1 = 0.045$ μM, $d_2 = 27.0$ μM, $d_3 = 0.0015$ μM, $d_4 = 0.9$ μM, and $d_5 = 0.18$ μM for the M146L cells (see Table 1).

3.3 Dissociation constants d_3 and d_5 are both modulated by mutant PS1

In this section, we show that parameters d_3 and d_5 have to decrease to fit the experimental data of P_O in M146L cells. We investigated the dependence of P_O on d_3 and d_5 by setting the other parameters to their typical values ($d_2 = 27.0$ μM and $d_4 = 0.9$ μM), according to the results

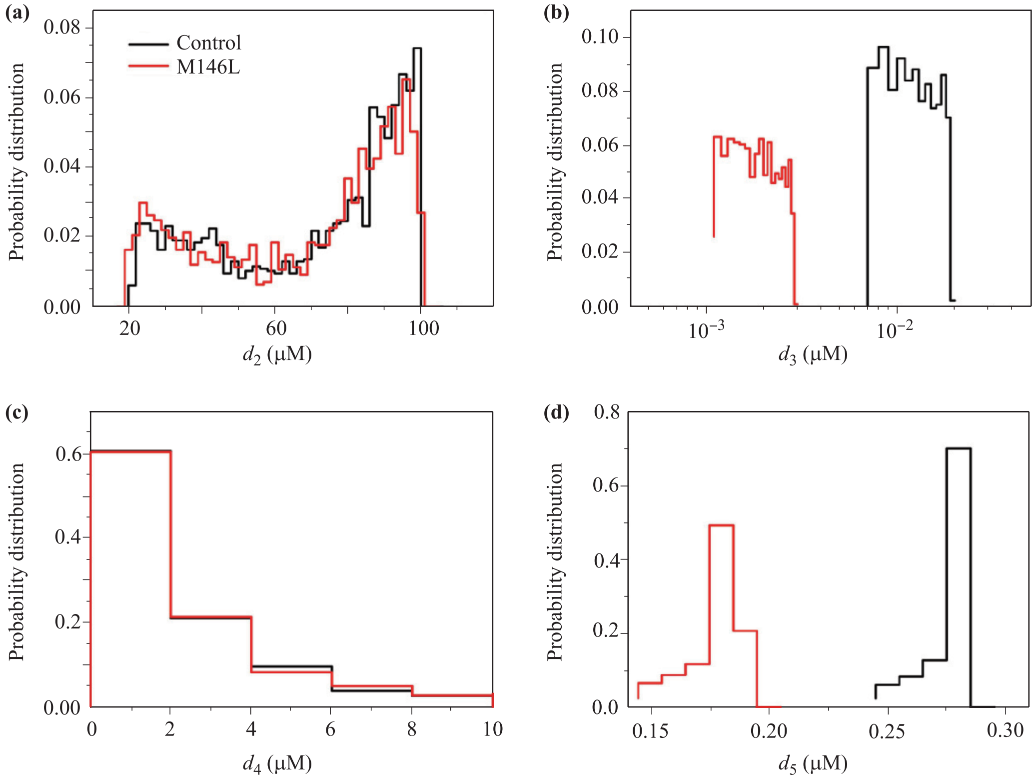

Fig. 5 Comparison of probability distributions of IP_3R model parameters between control and M146L cells after ignoring the parameter sets with low probability. **(a–d)** show the parameter distributions of d_2, d_3, d_4, and d_5, respectively. The black lines represent the control cells and the red lines represent the M146L cells.

shown in Fig. 5, with $C = 1$ μM.

First, we studied the dependence of P_O on d_3 and d_5 at a high concentration of IP$_3$, $I = 10$ μM. As plotted in Fig. 6(a), the almost vertical color bars indicate that P_O is mainly modulated by d_5, and is not sensitive to d_3. Thus, the experimental results of $P_O = 0.75$ for control cells and 0.86 for the M146L cells at $I = 10$ μM are located in the yellow and orange vertical bands, respectively.

We then studied the dependence of the open probability P_O of the channel on d_3 and d_5 at a low IP$_3$ concentration of $I = 33$ nM. As plotted in Fig. 6(b), P_O is sensitive not only to d_5, but also to d_3 at low I. Accordingly, the experimental results of $P_O = 0.27$ for the control cells and 0.76 for the M146L cells at $I = 33$ nM are located in the green and orange bands in Fig. 6(b), respectively.

Thus, the possible distributions of values of d_3 and d_5 represent the overlap areas of those specific bands in Figs. 6(a) and (b), represented by the black squares and circles, respectively. These black areas are exactly the high probability regions for parameters d_3 and d_5 shown in Figs. 5(b) and (d). The analysis of Fig. 6 showed that both d_3 and d_5 have changed in the M146L cells. The increased open channel probability P_O in the M146L cells mainly results from the change in the affinities of both IP$_3$ binding and activating Ca^{2+} binding.

3.4 Selection of optimal binding and unbinding rates

We next considered the channel binding and unbinding rates of a_2, b_3, and b_5, by applying the simulated annealing algorithm with Eqs. (3)–(5) and (7) to fit experimental data of τ_O and τ_C. Again, 2000 sets of the optimal parameters were obtained through 2000 independent runs of the simulated annealing algorithm. The resulting probability distributions of the fitted rates are plotted in Fig. 7. The distributions of a_2 for the control cells and mutant cells were almost identical and mainly concentrated in the interval 0–0.5 μM^{-1}·s^{-1}. However, Figs. 7(b) and (c) show that the most probable values of b_3 and b_5 are concentrated on two branches, both with one branch around 0.

As discussed above, the M146L mutation influences IP$_3$Rs by decreasing d_3 and d_5, leaving d_2 unchanged. Thus, we concluded that parameters a_2 and b_2 are unchanged. Thus, a typical value of $a_2 = 0.05$ μM^{-1}·s^{-1} is suggested.

We investigated how to determine b_3 and b_5 in the control and M146L cells. According to the experiment,

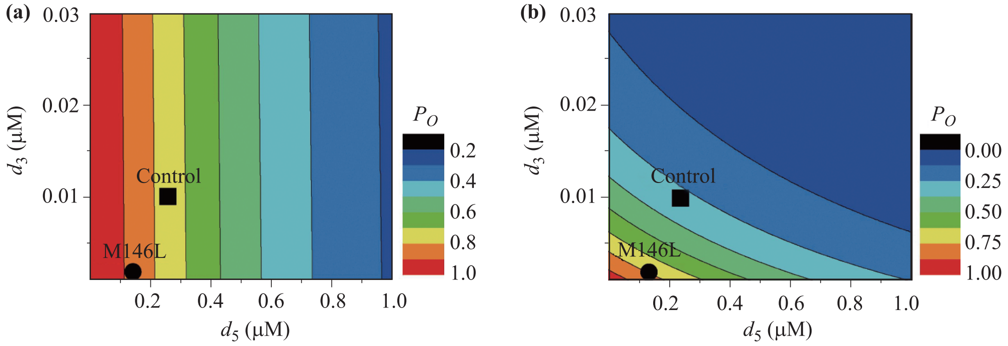

Fig. 6 The relationship between reaction dissociation constants d_3 and d_5 and the open probability P_O of the IP$_3$R channel. Here $d_2 = 27.0$ μM, $d_4 = 0.9$ μM, and calcium $(C) = 1$ μM, with IP$_3$ $(I) = 10$ μM **(a)** and 33 nM **(b)**.

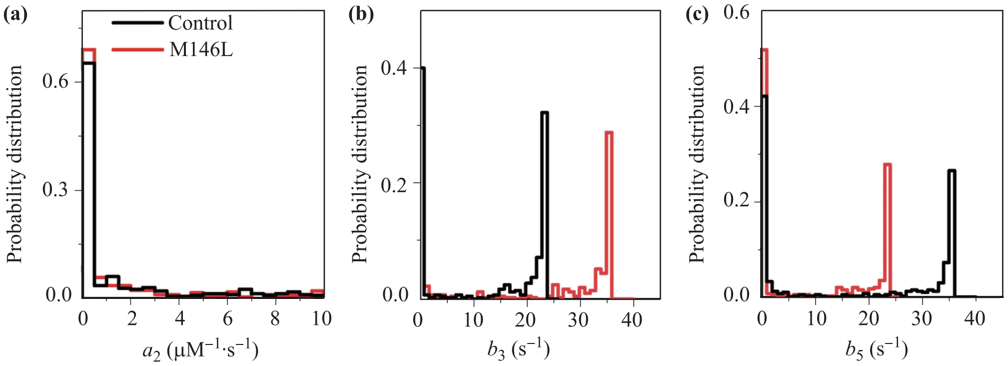

Fig. 7 Probability distributions of parameters a_2 **(a)**, b_3 **(b)**, and b_5 **(c)**. The black lines represent control cells and the red lines represent M146L cells.

for $C = 1$ μM and $I = 33$ nM, the values of τ_O and τ_C were $\tau_O = 11.5$ s and $\tau_C = 41.7$ s in the control cells, and $\tau_O = 31.9$ s and $\tau_C = 10.0$ s in the M146L cells. For $C = 1$ μM and $I = 10$ μM, the values of τ_O and τ_C were $\tau_O = 14.5$ s, $\tau_C = 4.1$ s in the control cells, and $\tau_O = 26.7$ s, $\tau_C = 3.6$ s in the M146L cells. Inserting these values into Eqs. (1)–(5) with the typical values for d_i selected above, we observed that $b_3 + b_5$ in the probability flux J should be around 35 s^{-1} in the control cells and 23 s^{-1} in the M146L cells. Because b_3 and b_5 might assume small values with large probability [see Figs. 7(b) and (c)], there are two simple ways to change b_3 and b_5. The first way is to change b_3 from approximately 35 s^{-1} in control cells to approximately 23 s^{-1} in the M146L cells, while keeping b_5 at approximately 0 for both cell types. The second way is to change b_5 from approximately 35 s^{-1} in the control cells to approximately 23 s^{-1} in the M146L cell, while keeping b_3 at approximately 0 for both cell types. Considering the relation $d_i = b_i/a_i$, and the fact that d_3 is much smaller than d_5 [see Figs. 5(b) and (d)], the natural choice is the second option, i.e., keeping the parameters a_3 and a_5 unchanged. This choice is also supported by Figs. 7(b) and (c) which also show that the parameter values of $b_5 = 35$ s^{-1} in the control cells and $b_5 = 23$ s^{-1} in the M146L cells, and b_3 at around 0 in both cell types, correspond to high distribution probabilities. Thus, the typical parameters were selected as $a_2 = 0.05$, $b_3 = 0.15$, and $b_5 = 35.4$ in the control cells, and as $a_2 = 0.05$, $b_3 = 0.02$, and $b_5 = 22.75$ in the M146L cells.

Finally, the typical values of all parameters are listed in Table 1. Table 1 indicates that the PS1 mutation in Sf9 cells mainly causes a decrease in the dissociation rates of Ca^{2+} and IP_3 from IP_3Rs, resulting in an increase in the affinities of IP_3 and activating Ca^{2+}. Figure 8 plots the curves of P_O, τ_O, and τ_C as a function of the calcium concentration for the control cells (black) and the M146L cells (red) at $I = 10$ μM and 33 nM, respectively. In the M146L cells, a large open probability was obtained, even at a small IP_3 stimulus of $I = 33$ nM, with a large mean open time.

4 Conclusions

In this study, we used a simulated annealing algorithm to find changes in the kinetic rate constants for a well-established mathematical model of the IP_3 receptor for M146L cells and SF9 control cells. Experimental data for the control and mutant cells were characterized by channel open probability P_O the mean open time τ_O, and the mean closed time τ_C. We discuss how the interaction of the presenilin mutation PS1 with the IP_3R channels modulates the gating dynamics of Ca^{2+} and IP_3 binding to and unbinding from IP_3Rs.

By comparing the typical model parameters for Sf9 control cells and the M146L mutant cells, we concluded that the PS1 mutation in Sf9 cells typically causes an increase in the channel's affinities for IP_3 and activating Ca^{2+} (i.e., a decrease in d_3 and d_5). More specifically, rather than modulating the binding rates, both the dissociation rates of IP_3 and activating Ca^{2+} become decreased in the M146L cells. Compared with the small decrease of dissociation rate b_5 from 35.4 s^{-1} in control cells to 22.76 s^{-1} in M146L cells, the decrease of b_3 from 0.15 s^{-1} in control cells to 0.025 s^{-1} in M146L cells is notable. Thus, the PS1 mutation decreases the IP_3 dissociation rate of IP_3R channels significantly in the M146L mutant cells.

Such decreases in dissociation rates mean that, once IP_3 messengers bind to the IP_3R or Ca^{2+} ions bind to the activating site of IP_3R, it is more difficult for IP_3 or

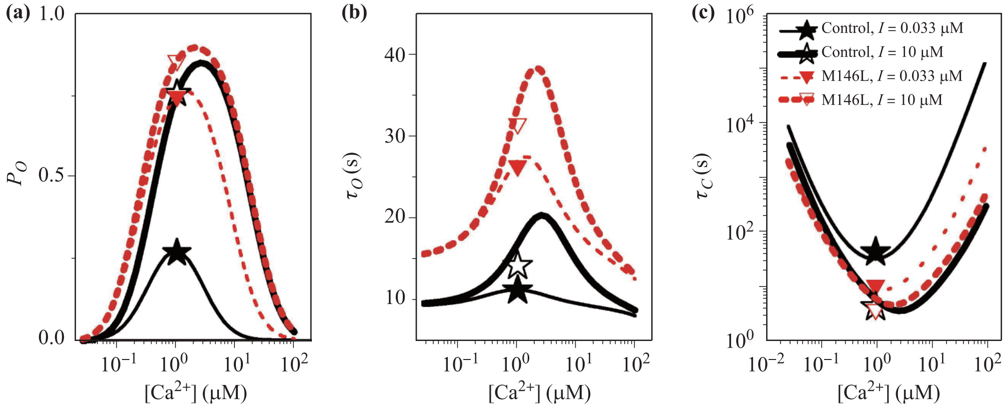

Fig. 8 Curves of P_O **(a)**, τ_O **(b)**, and τ_C **(c)** at different calcium (C) and IP_3 (I) concentrations. The solid black stars and the hollow black stars indicate the experimental data from the control cells at low and high IP_3 concentrations, respectively. The solid and hollow triangles indicate data from the M146L cells at high and low IP_3 concentrations, respectively [32]. The modeling results are represented by solid lines for the control cells and the dashed lines for the M146L cells.

activating Ca^{2+} to unbind from the IP_3R in the M146L mutant cells than in the control cells, allowing the channel subunit to stay in the active state (110) for longer (see Fig. 1). Thus, the channels in M146L cells show a longer open time τ_O and a shorter closed time τ_C with a larger open probability P_O, as shown in Fig. 8. The more easily opened IP_3Rs in M146 mutant cells will release more Ca^{2+} ions into the intracellular space from the ER pool, resulting in a high intracellular calcium concentration, as observed experimentally [23, 24].

In this study, the IP_3R channel gating dynamics were simulated using a modified DYK model. Such an IP_3R model was developed to account only for the equilibrium behaviors of IP_3R dynamics of P_O, τ_O, and τ_C. Other behaviors of channel gating, including modal gating [32] and the kinetic response to changes in ligand concentrations [33], have not been considered here because the larger number of parameters in more complex models cannot be constrained sufficiently by the limited experimental data (only the three parameters of P_O, τ_O and τ_C were available for the M146L mutant cells). We suggest, however, that the binding/dissociation rates of the more complex models should be similar, because they describe the same processes.

Ullah *et al.* considered some Markov chain models for ion channel gating of Aβ pores associated with Alzheimer's disease pathology [34]. They demonstrated the upregulation of gating of various Ca^{2+} release channels because of Aβ pores and showed that the extent and spatial range of such upregulation increased as Aβ pores with a low open probability and Ca^{2+} permeability transitioned into those with a high open probability and Ca^{2+} permeability. The present study was the first to study how a presenilin mutation in cells changes the gating dynamics of IP_3R channels to modulate the calcium signaling in Alzheimer's cells using a theoretical model. Our study offers a theoretical basis to explore the channel modulation mechanism of presenilin mutations in the cells of patients with Alzheimer's disease and may provide insights for the prevention and treatment of AD.

Acknowledgements We acknowledge support from the National Natural Science Foundation of China (Grant Nos. 31370830 and 11675134), the 111 Project (Grant No. B16029), and the China Postdoctoral Science Foundation (Grant No. 2016M602071).

References

1. M. Hutton and J. Hardy, The presenilins and Alzheimer's disease, *Hum. Mol. Genet.* 6(10), 1639 (1997)
2. J. Hardy, A hundred years of Alzheimer's disease research, *Neuron* 52(1), 3 (2006)
3. F. M. LaFerla and S. Oddo, Alzheimer's disease: Abeta, tau and synaptic dysfunction, *Trends Mol. Med.* 11(4), 170 (2005)
4. M. P. Mattson, Pathways towards and away from Alzheimer's disease, *Nature* 430(7000), 631 (2004)
5. C. Haass and D. J. Selkoe, Soluble protein oligomers in neurodegeneration: Lessons from the Alzheimer's amyloid beta-peptide, *Nat. Rev. Mol. Cell Biol.* 8(2), 101 (2007)
6. J. Hardy and D. J. Selkoe, The amyloid hypothesis of Alzheimer's disease: Progress and problems on the road to therapeutics, *Science* 297(5580), 353 (2002)
7. F. M. LaFerla, Calcium dyshomeostasis and intracellular signalling in Alzheimer's disease, *Nat. Rev. Neurosci.* 3(11), 862 (2002)
8. I. F. Smith, K. N. Green, and F. M. LaFerla, Calcium dysregulation in Alzheimer's disease: Recent advances gained from genetically modified animals, *Cell Calcium* 38(3–4), 427 (2005)
9. J. Herms, I. Schneider, I. Dewachter, N. Caluwaerts, H. Kretzschmar, and F. Van Leuven, Capacitive calcium entry is directly attenuated by mutant presenilin-1, independent of the expression of the amyloid precursor protein, *J. Biol. Chem.* 278(4), 2484 (2003)
10. M. A. Leissring, B. A. Paul, I. Parker, C. W. Cotman, and F. M. LaFerla, Alzheimer's presenilin-1 mutation potentiates inositol 1, 4, 5-trisphosphate-mediated calcium signaling in Xenopus oocytes, *J. Neurochem.* 72(3), 1061 (1999)
11. I. F. Smith, B. Hitt, K. N. Green, S. Oddo, and F. M. LaFerla, Enhanced caffeine-induced Ca^{2+} release in the 3xTg-AD mouse model of Alzheimer's disease, *J. Neurochem.* 94(6), 1711 (2005)
12. G. E. Stutzmann, Calcium dysregulation, IP_3 signaling, and Alzheimer's disease, *Neuroscientist* 11(2), 110 (2005)
13. G. E. Stutzmann, A. Caccamo, F. M. LaFerla, and I. Parker, Dysregulated IP_3 signaling in cortical neurons of knock-in mice expressing an Alzheimer's-linked mutation in presenilin1 results in exaggerated Ca^{2+} signals and altered membrane excitability, *J. Neurosci.* 24(2), 508 (2004)
14. J. K. Foskett, C. White, K. H. Cheung, and D. O. D. Mak, Inositol trisphosphate receptor Ca^{2+} release channels, *Physiol. Rev.* 87(2), 593 (2007)
15. M. J. Berridge, M. D. Bootman, and H. L. Roderick, Calcium signaling: Dynamics, homeostasis and remodeling, *Nat. Rev. Mol. Cell Biol.* 4(7), 517 (2003)
16. K. N. Green, A. Demuro, Y. Akbari, B. D. Hitt, I. F. Smith, I. Parker, and F. M. LaFerla, SERCA pump activity is physiologically regulated by presenilin and regulates amyloid beta production, *J. Cell Biol.* 181(7), 1107 (2008)

17. S. Chakroborty, I. Goussakov, M. B. Miller, and G. E. Stutzmann, Deviant ryanodine receptor-mediated calcium release resets synaptic homeostasis in presymptomatic 3xTg-AD mice, *J. Neurosci.* 29(30), 9458 (2009)

18. G. E. Stutzmann, I. Smith, A. Caccamo, S. Oddo, F. M. Laferla, and I. Parker, Enhanced ryanodine receptor recruitment contributes to Ca^{2+} disruptions in young, adult, and aged Alzheimer's disease mice, *J. Neurosci.* 26(19), 5180 (2006)

19. H. Qi and J. Shuai, Alzheimer's disease via enhanced calcium signaling caused by the decrease of endoplasmic reticulum–mitochondrial distance, *Med. Hypotheses.* 89, 28 (2016)

20. H. Qi, L. Li, and J. Shuai, Optimal microdomain crosstalk between endoplasmic reticulum and mitochondria for Ca^{2+} oscillations, *Sci. Rep.* 5, 7984 (2015)

21. N. Hirashima, R. Etcheberrigaray, S. Bergamaschi, M. Racchi, F. Battaini, G. Binetti, S. Govoni, and D. L. Alkon, Calcium responses in human fibroblasts: a diagnostic molecular profile for Alzheimer's disease, *Neurobiol. Aging.* 17(4), 549 (1996)

22. E. Ito, K. Oka, R. Etcheberrigaray, T. J. Nelson, D. L. McPhie, B. Tofel-Grehl, G. E. Gibson, and D. L. Alkon, Internal Ca^{2+} mobilization is altered in fibroblasts from patients with Alzheimer disease, *Proc. Natl. Acad. Sci. USA* 91(2), 534 (1994)

23. K. H. Cheung, D. Shineman, M. Muller, C. Cardenas, L. Mei, J. Yang, T. Tomita, T. Iwatsubo, V. M. Lee, and J. K. Foskett, Mechanism of Ca^{2+} disruption in Alzheimer's disease by presenilin regulation of $InsP_3$ receptor channel gating, *Neuron.* 58(6), 871 (2008)

24. K. H. Cheung, L. Mei, D. O. D. Mak, I. Hayashi, T. Iwatsubo, D. E. Kang, and J. K. Foskett, Gain-of-function enhancement of $InsP_3$ receptor modal gating by familial Alzheimer's disease-linked presenilin mutants in humancells and mouse neurons, *Sci. Signal.* 3(114), ra22 (2010)

25. G. W. De Young, and J. Keizer, A single-pool inositol 1, 4, 5-trisphosphate- receptor-based model for agonist-stimulated oscillations in Ca^{2+} concentration, *Proc. Natl. Acad. Sci. USA* 89(20), 9895 (1992)

26. J. Sneyd and J. Dufour, A dynamic model of the type-2 inositol trisphosphate receptor, *Proc. Natl. Acad. Sci. USA* 99(4), 2398 (2002)

27. D. O. D. Mak, S. M. J. McBride, and J. K. Foskett, Spontaneous channel activity of the inositol 1, 4, 5-trisphosphate ($InsP_3$) receptor ($InsP_3R$): Application of allosteric modeling to calcium and $InsP_3$ regulation of $InsP_3R$ single-channel gating, *J. Gen. Physiol.* 122(5), 583 (2003)

28. J. Shuai, J. E. Pearson, J. K. Foskett, D. O. D. Mak, and I. Parker, A kinetic model of single and clustered IP_3 receptors in the absence of Ca^{2+} feedback, *Biophys. J.* 93(4), 1151 (2007)

29. J. W. Shuai, D. P. Yang, J. E. Pearson, and S. Rüdiger, An investigation of models of the IP_3R channel in Xenopus oocyte, *Chaos* 19(3), 037105 (2009)

30. G. Ullah, D. O. Daniel Mak, and J. E. Pearson, A data-driven model of a modal gated ion channel: The inositol 1, 4, 5-trisphosphate receptor in insect Sf9 cells, *J. Gen. Physiol.* 140(2), 159 (2012)

31. B. A. Bicknell, and G. J. Goodhill, Emergence of ion channel modal gating from independent subunit kinetics, *Proc. Natl. Acad. Sci. USA* 113(36), E5288 (2016)

32. L. Ionescu, C. White, K. H. Cheung, J. Shuai, I. Parker, J. E. Pearson, J. K. Foskett, and D. O. D. Mak, Mode switching is the major mechanism of ligand regulation of InsP3 receptor calcium release channels, *J. Gen. Physiol.* 130(6), 631 (2007)

33. D. O. D. Mak, J. E. Pearson, K. P. C. Loong, S. Datta, M. Fernández-Mongil, and J. K. Foskett, Rapid ligand-regulated gating kinetics of single inositol 1, 4, 5-trisphosphate receptor Ca^{2+} release channels, *EMBO Rep.* 8(11), 1044 (2007)

34. G. Ullah, A. Demuro, I. Parker, and J. E. Pearson, Analyzing and modeling the kinetics of amyloid beta pores associated with Alzheimer's disease pathology, *PLoS One* 10(9), e0137357 (2015)